Bursts of Fast Propagating Swarms of Induced Earthquakes at the Groningen Gas Field

Krittanon Sirorattanakul[*1], John D. Wilding[1], Mateo Acosta[1], Yuexin Li[1], Zachary E. Ross[1], Stephen J. Bourne[2], Jan van Elk[3], and Jean-Philippe Avouac[1,4]

Abstract

Gas extraction from the Groningen gas reservoir, located in the northeastern Netherlands, has led to a drop in pressure and drove compaction and induced seismicity. Stress-based models have shown success in forecasting induced seismicity in this particular context and elsewhere, but they generally assume that earthquake clustering is negligible. To assess earthquake clustering at Groningen, we generate an enhanced seismicity catalog using a deep-learning-based workflow. We identify and locate 1369 events between 2015 and 2022, including 660 newly detected events not previously identified by the standard catalog from the Royal Netherlands Meteorological Institute. Using the nearest-neighbor distance approach, we find that 72% of events are background independent events, whereas the remaining 28% belong to clusters. The 55% of the clustered events are swarm-like, whereas the rest are aftershock-like. Among the swarms include five newly identified sequences propagating at high velocities between 3 and 50 km/day along directions that do not follow mapped faults or existing structures and frequently exhibit a sharp turn in the middle of the sequence. The swarms occurred around the time of the maximum compaction rate between November 2016 and May 2017 in the Zechstein layer, above the anhydrite caprock, and well-above the directly induced earthquakes that occur within the reservoir and caprock. We suggest that these swarms are related to the aseismic deformation within the salt formation rather than fluids. This study suggests that the propagating swarms do not always signify fluid migration.

Cite this article as Sirorattanakul, K., J. D. Wilding, M. Acosta, Y. Li, Z. E. Ross, S. J. Bourne, J. van Elk, and J.-P. Avouac (2024). Bursts of Fast Propagating Swarms of Induced Earthquakes at the Groningen Gas Field, *Seismol. Res. Lett.* **XX**, 1–17, doi: 10.1785/0220240107.

Supplemental Material

Introduction

Industrial activities, such as gas extraction, wastewater disposal, hydraulic stimulation, geothermal energy production, carbon dioxide sequestration, and water impoundment from dams can produce substantial stress changes in the Earth's crust that can induce seismicity (Ellsworth, 2013; Grigoli *et al.*, 2017; Keranen and Weingarten, 2018; Atkinson *et al.*, 2020; Wu *et al.*, 2022; Moein *et al.*, 2023). The induced earthquakes can occasionally reach magnitudes of 5 or above, with hypocenters that are often shallower than those of natural seismicity (Hough, 2015), making them capable of damaging nearby structures (Clayton *et al.*, 2016). Management of the seismic risks to be within an acceptable level is critical for successful operations.

Induced earthquakes, which exclude background earthquakes driven by tectonics and other natural causes of stress changes, can generally be grouped into two modes based on their clustering behaviors. The first mode includes independent events that are driven directly by the stress changes due to the large-scale human activity, whether from changes in pore pressure as the fluid diffuses (Hubbert and Rubey, 1959; Nur and Booker, 1972) or long-range poroelastic stress changes (Segall, 1989; Segall *et al.*, 1994; Goebel *et al.*, 2017; Zhai *et al.*, 2019). These events are expected to follow a Poisson process, generally nonhomogeneous, with time-varying rates governed by stress changes (Dempsey and Suckale, 2017; Dahm and Hainzl, 2022; Luu *et al.*, 2022; Smith *et al.*, 2022; Acosta *et al.*, 2023). The second mode includes the

1. Division of Geological and Planetary Sciences, California Institute of Technology, Pasadena, California, U.S.A., https://orcid.org/0000-0003-2310-8447 (KS); https://orcid.org/0000-0002-0914-2078 (JDW); https://orcid.org/0000-0002-0098-7912 (MA); https://orcid.org/0000-0002-0160-7504 (YL); https://orcid.org/0000-0002-6343-8400 (ZER); https://orcid.org/0000-0002-3060-8442 (J-PA); 2. Shell Global Solutions International B.V., Amsterdam, The Netherlands, https://orcid.org/0000-0003-2925-8411 (SJB); 3. Nederlandse Aardolie Maatschappij B.V., Assen, The Netherlands; 4. Department of Mechanical and Civil Engineering, California Institute of Technology, Pasadena, California, U.S.A.

*Corresponding author: ksirorat@caltech.edu

clustered events that appear close in space and time with an independent event and often occur as aftershocks or more occasionally as foreshocks, as also observed in natural seismicity (Ogata, 1988). Mechanistically, these events are triggered by stress changes imparted by a previous earthquake rather than the industrial operations. Aftershocks generally follow well-known patterns, including the decay of their occurrence rates with time as a power law (Omori, 1894; Utsu, 1961), and a scaling in which the largest aftershock is approximately 1.2 magnitude unit lower than the mainshock (Richter, 1958). Clustered events may occasionally deviate from this well-defined pattern and occur as enigmatic bursts of small-magnitude earthquakes without an identifiable mainshock, referred to as swarms (Mogi, 1963). They often exhibit migratory patterns (Audin *et al.*, 2002; Hainzl and Fischer, 2002; Chen and Shearer, 2011) and are a manifestation of underlying aseismic processes such as spontaneous slow-slip events (Lohman and McGuire, 2007; Passarelli *et al.*, 2015; Gualandi *et al.*, 2017; Jiang *et al.*, 2022), fluid pressure diffusion (Shapiro *et al.*, 1997; Audin *et al.*, 2002; Hainzl and Fischer, 2002; Shelly *et al.*, 2013; Ruhl *et al.*, 2016; Ross and Cochran, 2021), or a complex interaction of both (Dublanchet and De Barros, 2021; Sirorattanakul *et al.*, 2022; Yukutake *et al.*, 2022). Clustering is generally small in induced seismicity with a proportion of clustered events generally less than 30% (Zaliapin and Ben-Zion, 2016; Cochran *et al.*, 2020; Karimi and Davidsen, 2023), whereas clusters typically represent up to 70% of natural seismicity (Zaliapin and Ben-Zion, 2013a). Swarms have also been observed in the context of induced seismicity for which they are generally ascribed to fluid migration (Ake *et al.*, 2005; Baisch *et al.*, 2006; Albaric *et al.*, 2014; Kwiatek *et al.*, 2019).

In this study, we take advantage of publicly available seismic datasets related to seismicity induced by production in the Groningen gas field in the northeastern Netherlands (Dost *et al.*, 2017; Willacy *et al.*, 2019; Oates *et al.*, 2022) to investigate the degree of clustering and the possible mechanisms involved. We produce an enhanced seismicity catalog for the region using a deep-learning-based workflow. The improved catalog reveals many previously unidentified events, which enables more extensive statistical analysis of earthquake clusters. The newly detected events include five distinct swarm sequences propagating at high velocity between 3 and 50 km/day.

The Groningen Gas Field, Overview of Previous Studies of Induced Seismicity

The Groningen gas field is the largest in western Europe (Fig. 1), with an initial gas reserve of approximately 2913 billion cubic meters (BCM; Burkitov *et al.*, 2016). The gas comprises 85% of methane (CH_4), 14% of nitrogen (N_2), and 1% of carbon dioxide (CO_2) (Stäuble and Milius, 1970; Burkitov *et al.*, 2016). The reservoir lies at a depth of between 2.6 and 3.2 km and spans approximately 35 km east–west and 50 km north–south as a part of the Upper Rotlingend Group composed of interbedded Slochteren sandstone and Ten Boer claystone units. Its thickness varies substantially from 90 m in the southeast to 300 m in the northwest. The coal layers, in the underlying Pennsylvanian Carboniferous limestone, are the source of the gas. The reservoir is sealed by an overlying thick and impermeable caprock of anhydrite and evaporite layers of the Permian Zechstein group, an aquifer toward the north, and a system of normal faults (de Jager and Visser, 2017). Because of the limited connection with the surrounding groundwater, gas extraction has led to significant pressure depletion from 34.68 MPa, close to hydrostatic pressure (Burkitov *et al.*, 2016), to <10 MPa (Meyer *et al.*, 2023), which resulted in the surface subsidence of almost 40 cm (Smith *et al.*, 2019).

Although the field has been in production since 1963, induced seismicity did not start until 1991 (Dost *et al.*, 2017). From 1991 to 2013, the number of earthquakes increased exponentially, prompting significant efforts to deploy additional monitoring instruments. The first regional network in operation since 1995 consisted of eight stations, each with three-component geophones at four different depth levels (50, 100, 150, and 200 m) and a surface accelerometer. Several upgrades of the network followed. In a major upgrade late 2014, 59 additional stations were deployed, significantly improving seismic activity detection (Dost *et al.*, 2017). Most earthquakes align well with one of the >1100 normal faults mapped by seismic techniques that offset the gas reservoir (Visser and Solano Viota, 2017) and are located primarily within the reservoir (Willacy *et al.*, 2019) or in the overburden (Smith *et al.*, 2020). They are thought to be driven primarily by poroelastic stresses induced by bulk reservoir volume decrease (Bourne *et al.*, 2014; Dempsey and Suckale, 2017; Candela *et al.*, 2019; Smith *et al.*, 2022) or by stress concentration around faults offsetting the reservoir resulting from compaction (Bourne *et al.*, 2014; Buijze *et al.*, 2017; Van Wees *et al.*, 2018). The largest earthquake to date is the 2012 M_w 3.6 Huizinge earthquake, which sparked public concerns and prompted the regulators to request ramping down of production and to eventually shut it down long before exhaustion of the gas reserve (de Waal *et al.*, 2015; van Thienen-Visser and Breunese, 2015; Muntendam-Bos *et al.*, 2017).

In recent years, many researchers have developed computationally efficient models to forecast occurrence rates of induced seismicity based on stress changes from industrial operations (Segall and Lu, 2015; Bourne and Oates, 2017; Dempsey and Suckale, 2017; Bourne *et al.*, 2018; Langenbruch *et al.*, 2018; Candela *et al.*, 2019; Zhai *et al.*, 2019; Richter *et al.*, 2020; Candela *et al.*, 2022; Dahm and Hainzl, 2022; Heimisson *et al.*, 2022; Kühn *et al.*, 2022; Smith *et al.*, 2022; Acosta *et al.*, 2023; Kim and Avouac, 2023). One major limitation of these stress-based models is that they do not account for interactions between earthquakes that may lead to secondary triggering and appear as clustered events. Although induced earthquakes tend to have fewer clustered events than natural earthquakes, their

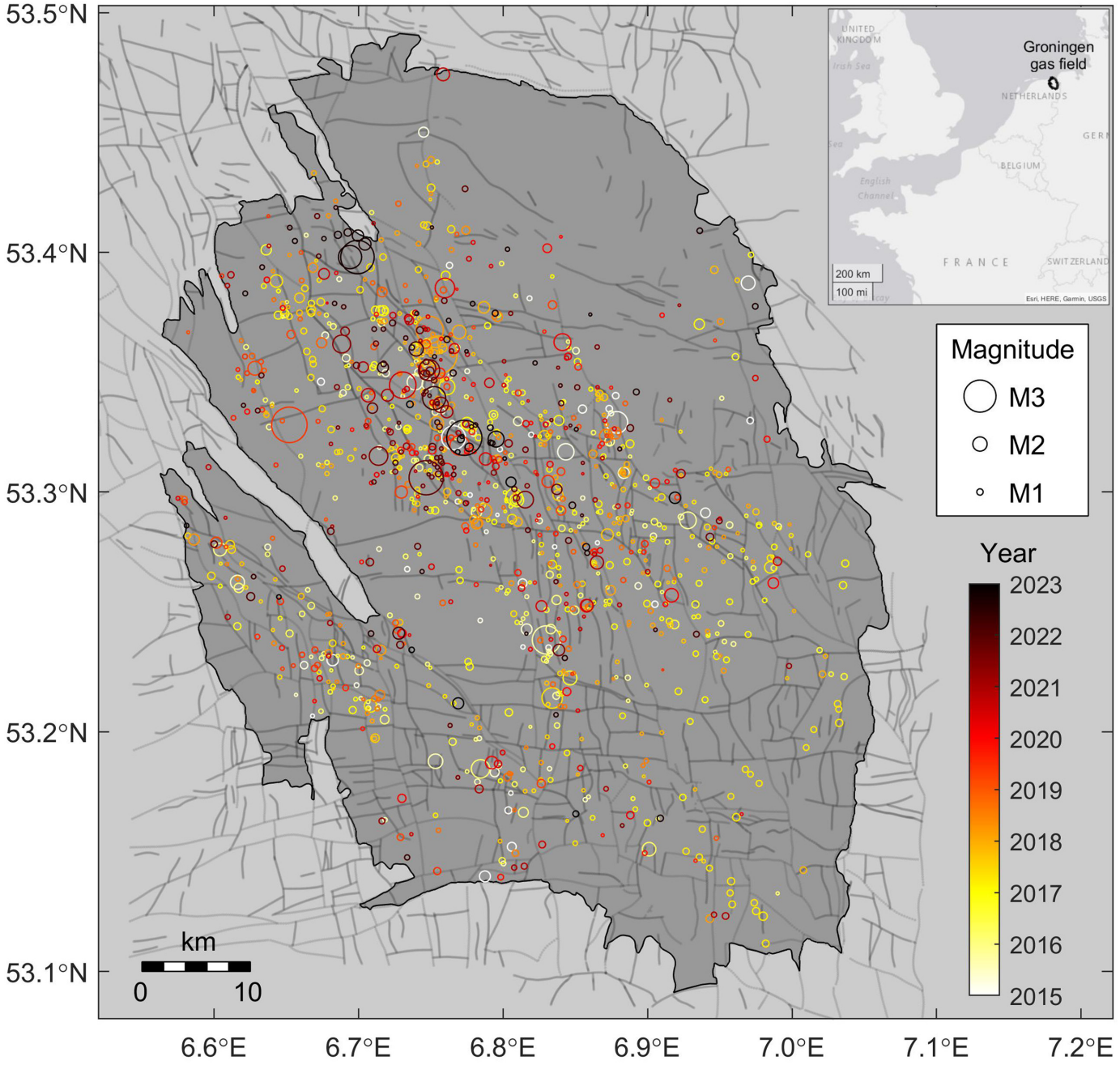

proportions can be >50% depending on the geological settings, which is nonnegligible (Zaliapin and Ben-Zion, 2016). A better understanding of clustering behaviors of induced seismicity can lead to further improvements in these models.

Figure 1. Map of induced seismicity in the Groningen gas field from 2015 to 2023 that was detected and located in this study using a deep-learning-based workflow. Circles show the events with size representing the local magnitude and color representing the occurrence time. The black line shows the outline of the reservoir. Gray lines show the mapped faults. The inset shows the location of the gas field within Europe. The color version of this figure is available only in the electronic edition.

Data and Methods

Enhanced seismicity catalog generation

The Royal Netherlands Meteorological Institute (KNMI) has been the authoritative governmental institution responsible for maintaining a seismicity catalog for the area surrounding the Groningen gas field since 1995. To supplement the KNMI catalog, we use a recently developed deep-learning-based workflow to build an enhanced high-resolution seismicity catalog (Data S1, available in the supplemental material to this article) between 2015 and 2022 covering the domain spanning latitude 53.05°–53.50° N and longitude 6.48°–7.05° E. As summarized subsequently, the workflow consists of multiple steps, including phase picking, phase association, earthquake location, and magnitude estimation.

Waveform data from seismic stations in the NL and NR networks located within our domain are used in this analysis (Fig. S1). We first apply the PhaseNet automated phase-picking algorithm based on a convolutional neural network to detect *P*- and *S*-wave arrivals (Zhu and Beroza, 2019). The algorithm accepts one- or three-component waveform data as input and outputs a list of timestamped *P*- or *S*-wave arrival times (Data S2). We use the standard model included with the PhaseNet distribution, which was trained on California data based on manual picks from seismic analysts at the Northern California Earthquake Data Center but has been shown to effectively generalize to other regions worldwide, including Hawaii (Wilding *et al.*, 2023), Italy (Tan *et al.*, 2021), and Arkansas, United States (Park *et al.*, 2020). The initial iteration of the catalog, spanning from mid-2015 to 2018, includes picking from both surface and borehole seismometers. However, when we expand the catalog to include the first few months of 2015 and from 2019 to 2022, we only apply PhaseNet to surface sensors for computational efficiency. In addition, for instruments with a sampling rate greater than 100 Hz, we decimate waveform data to 100 Hz per PhaseNet requirements. The output from PhaseNet also has probability labels between 0 and 1, indicating confidence in the pick. We set a probability threshold of 0.3 and remove picks below this confidence threshold.

The *P*- and *S*-arrival picks are then associated into discrete earthquake events using the Gaussian Mixture Model Associator, GaMMA (Zhu *et al.*, 2022). GaMMA probabilistically assigns clusters of *P* and *S* picks to individual sources based on identified hyperbolic moveouts and iterates those assignments using the expectation–maximization process. The main parameters controlling the association process are the maximum time ε between two picks to be considered as a neighbor of the other and the scalar *P*- and *S*-wave velocity used to backproject arrivals. Even though GaMMA uses a uniform velocity model, it can account for travel-time errors in backprojection due to 3D variation of the velocity model by allowing large uncertainty in arrival times during the clustering stage. We test different parameters and identify the best set of parameters as those that include the greatest number of events previously identified by KNMI. The best combination of parameters uses ε of 3 s, a *P*-wave velocity of 3.0 km/s, and an *S*-wave velocity of 1.8 km/s. With this set of parameters, GaMMA identifies 709 out of 739 events in the KNMI catalog over the same spatial and temporal coverage. After the association, we filter out previously unidentified events with fewer than 5 *P* or *S* picks and are left with 2591 events. Finally, we manually inspect waveforms of all newly identified events and remove the spurious picks resulting in 1369 events, including 660 newly detected events (Figs. S2, S3).

The events are then located with a modified version of the Hypocenter inversion with Stein Variational Inference and physics-informed neural networks (HypoSVI) program (Smith *et al.*, 2021), adapted to allow for a 3D velocity model. The velocity model of the Groningen region used in this study was produced by Nederlandse Aardolie Maatschappij (NAM) from seismic reflection, seismic refraction, sonic log, and well-core samples (Nederlandse Aardolie Maatschappij, 2017). Because HypoSVI inverts for the full posterior distribution of an earthquake location, the algorithm also outputs associated location uncertainties. Compared with the KNMI catalog, we find approximately 40 mismatched events. Most of these events are located near the edges of the velocity model domain by both our algorithm and by KNMI. They are most likely affected by the low number of picks on stations within the velocity model domain and increased picking errors for arrivals with a lower signal-to-noise ratio. To maintain the integrity of the catalog, we manually assign the locations of these events to those provided by the KNMI, which can be identified by their depth of exactly 3 km. Events with picks only from the surface geophones have larger depth uncertainty, as evidenced by several surface-sensor-only events with depths far from the reservoir. These depths can be considered artifacts of the data downsampling process. We have also compared the epicentral (horizontal) locations derived using picks from all sensors and only from surface sensors. They are largely unaffected by excluding the picks from the borehole sensors.

Local earthquake magnitudes (M_L) are calculated with the same procedure used by the KNMI (NORSAR, 2018), which can be calculated using the following equation:

$$M_L = \log_{10} A + 1.33 \log_{10} R + 0.00139R + 0.424, \quad (1)$$

in which A is the amplitude measurement in millimeters on a simulated Wood–Anderson seismometer of the deepest available borehole sensor for a given station and R is the source–receiver distance in kilometers. The amplitudes are measured as the peak signal amplitude of the waveform (absolute value). Although it is possible to convert local magnitude to moment magnitude using the relation derived by Dost *et al.* (2018), we restrict our analysis to local magnitude.

Clustering analysis

To analyze the clustering behaviors of seismicity in the Groningen gas field, we apply the nearest-neighbor distance approach (Zaliapin and Ben-Zion, 2013a,b) to the enhanced seismicity catalog. We consider only events located within the boundary of the Groningen gas field that are larger than the completeness magnitude (M_c) of 0.5. For each event j in the catalog, we search for the preceding event i that is most likely to be the parent (mainshock) of event j. The proximity distance between any event pair (i, j) can be quantified using a space–time–magnitude metric normalized by the magnitude of the parent event (Baiesi and Paczuski, 2004; Zaliapin *et al.*, 2008) defined as follows:

$$\eta_{ij} = t_{ij}(r_{ij})^{d_f} 10^{-b(m_i - M_c)}, \quad (2)$$

in which $t_{ij} = t_j - t_i$ is the time between the event pair, r_{ij} is the distance between the epicenters of the event pair, d_f is the fractal dimension of earthquake epicenters taken to be 1.6 (Zaliapin and Ben-Zion, 2013a), b is the Gutenberg–Richter b-value of the frequency–magnitude distribution, and m_i is the magnitude of event i. Because depth uncertainty is large, we do not include depths in the proximity distance calculations for our analysis. However, we tested the effect of including depths in the analysis (see the Clustering behaviors section) and find no significant changes to the conclusions presented in the following sections.

For each event j, the event i^* with the smallest proximity distance η_{ij} is the nearest neighbor and hence most likely to be the parent of event j. The results can be expanded to two dimensions as rescaled time T_j and rescaled distance R_j, defined as follows (Zaliapin and Ben-Zion, 2013a):

$$T_j = t_{i^*j}\, 10^{-\frac{b}{2}(m_{i^*} - M_c)}, R_j = (r_{i^*j})^{d_f} 10^{-\frac{b}{2}(m_{i^*} - M_c)}. \quad (3)$$

The distribution of nearest-neighbor distance η_j is expected to be bimodal. The first mode has the independent events represented by a time-stationary, space-inhomogeneous Poisson process concentrating along $\log_{10} T_j + \log_{10} R_j = \text{constant}$. The second mode has the clustered events with considerably smaller T_j and R_j, constituting foreshock–mainshock–aftershock sequences and swarms (Zaliapin *et al.*, 2008; Zaliapin and Ben-Zion, 2013a). The separation between the two modes can be approximated by a 1D Gaussian mixture model applied on η_j (Hicks, 2011) using MATLAB *fitgmdist* function. The mode separator η_0 is chosen to be where the probability density function of the two modes intersects. We consider events with $\eta_j \geq \eta_0$ to be independent events and $\eta_j < \eta_0$ to be clustered events (Zaliapin and Ben-Zion, 2013a).

The nearest-neighbor distance approach was originally analyzed for an epidemic-type aftershock sequence model (Ogata, 1988) with an assumption that the independent events follow a time-stationary, space-inhomogeneous Poisson process (Zaliapin *et al.*, 2008). In the case of induced seismicity, we expect the background Poisson rates of independent events to be inhomogeneous in time as modulated by injection or extraction rates. To test the effectiveness of the nearest-neighbor distance approach for induced seismicity and the robustness of the estimated mode separator η_0 a posteriori, we take events with $\eta_j \geq \eta_0$, create 100 shuffled catalogs by randomly permuting the order of the magnitudes and locations, and calculate nearest-neighbor distances for events in these shuffled catalogs, similar to those done in Karimi and Davidsen (2023). Because the shuffling removes any clusters while preserving the seismicity rate and spatial distribution, the distribution of nearest-neighbor distances of these shuffled events reflects the true distribution of the independent mode, and hence the majority of events should have $\eta_{j,\text{shuffled}} \geq \eta_0$ if the chosen η_0 is appropriate. Unlike in Karimi and Davidsen (2023), by shuffling only events with $\eta_j \geq \eta_0$, we reduce bias of the clustered events on the temporal rate of independent events. In principle, we can also completely remove the time clustering by sampling new times from a uniform distribution (Zaliapin and Ben-Zion, 2020), but then we would also remove any time-inhomogeneous nature of the independent events.

Furthermore, we also evaluate the relative variability of the interevent times distribution using the coefficient of variation (CoV) defined as the ratio of its standard deviation and its mean. Random processes (Poissonian) are expected to have CoV in order of unity. Larger CoV suggests the presence of clustering, whereas smaller CoV suggests periodic behavior. For a given η_0, the CoV can be used to evaluate whether the independent events are Poissonian. If the chosen η_0 is too small, events with $\eta_j \geq \eta_0$ would include some clustered events, and hence the CoV would become significantly greater than one. In contrary to the shuffling analysis, which evaluates the upper bound of the appropriate η_0, the CoV evaluates its lower bound. Combining the two metrics effectively allows constraining the range of η_0 that characterizes the mode separation.

We additionally use the Schuster spectrum method (Ader and Avouac, 2013) to verify that, once clustered events are removed based on the chosen value of the mode separator η_0, the remaining events are consistent with an inhomogeneous Poisson process. The method is based on the Schuster tests (Schuster, 1897), which evaluate the amount of seismicity rate variations for a given period. By calculating the Schuster p-value for different periods, we construct a Schuster spectrum and compare it with the expectation for a Poisson process. This procedure aids in verification of the quality of the declustering.

To further study the relationship between events, we create a spanning tree by connecting each event to its most likely parent. The strength of each link is inversely proportional to the nearest-neighbor distance η_j. By removing weak links with $\eta_j \geq \eta_0$, we create a spanning forest consisting of single-event trees with no links and other multievent clusters (Zaliapin and Ben-Zion, 2013a). The independent events previously identified include the singles and the first event from each cluster. We can calculate the average leaf depth for each cluster by averaging the number of links needed to connect events without children to the first event or the root (Zaliapin and Ben-Zion, 2013b). Swarm-like sequences have large average leaf depths, whereas foreshock–mainshock–aftershock sequences have small average leaf depths.

Results

Catalog overall properties

Compared to the standard catalog from the KNMI, our deep-learning-based workflow enables us to increase the number of detected events between 2015 and 2022 from 739 to 1369. In total, 709 events from the KNMI catalog were identified by our workflow, leaving only 30 events unidentified by our method.

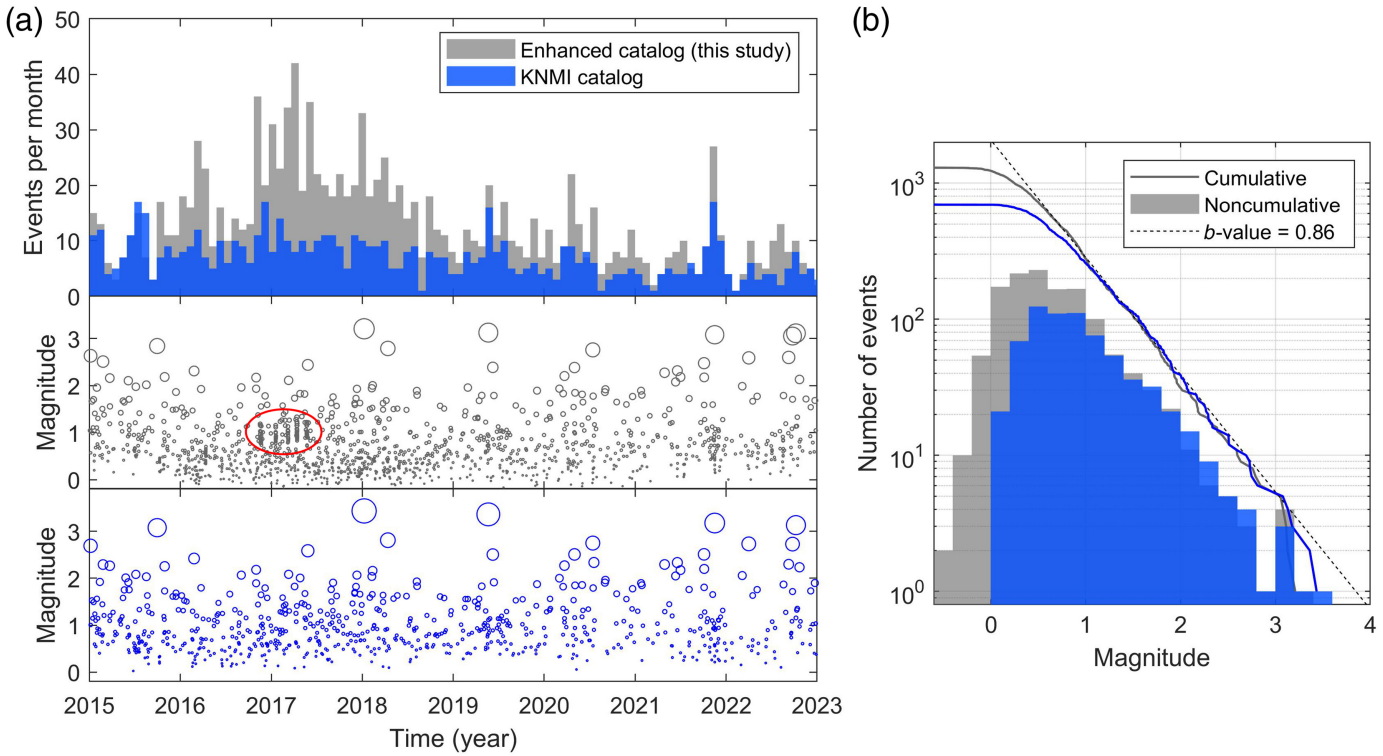

Figure 2. Enhanced seismicity catalog. (a) Comparison between our enhanced seismicity catalog and the standard catalog from the Royal Netherlands Meteorological Institute (KNMI). The top panel compares the number of detected events per month. The middle panel shows the distribution of event magnitude versus time for the enhanced catalog. The red circle highlights the five newly detected swarm sequences. The bottom panel is the same as the middle but for the KNMI catalog. (b) Frequency–magnitude distribution from the two catalogs. The dashed line represents the Gutenberg–Richter exponential distribution with the *b*-value slope of 0.86 estimated from the enhanced catalog using the *b*-Positive method (van der Elst, 2021). The completeness magnitude (M_c) of the enhanced catalog is estimated to be approximately 0.5. The color version of this figure is available only in the electronic edition.

The 1297 events are located within the horizontal extent of the gas field, which we use for the analysis hereafter.

Despite being automatically generated products, our events display good agreement in both the locations and magnitudes with the KNMI catalog (Fig. S4). The horizontal location differences for events with $M_L \geq 0.5$ are less than 675 m on average. Most events with large location differences are either located near the edge of the available velocity model or small-magnitude events where arrival picks have large uncertainty. The magnitude differences are less than 0.1 magnitude unit on average. Only 78 events (12%) have magnitude differences greater than 0.2 magnitude units. There is one M_L 3 event that is presented in our catalog but not in the KNMI catalog. Because that event is located close the edge of the velocity model, the arrival picks may have large uncertainty and bias its location and, therefore, its magnitude. Our catalog also reports depth rather than a fixed depth of 3 km, as the KNMI catalog does. In comparison to the catalog by Willacy *et al.* (2019), which utilizes full-waveform inversion to determine the event location, the horizontal location differences for events with $M_L \geq 0.5$ decrease slightly to a mean value of 563 m (Fig. S5). We have refined the depth determination by including time picks from the borehole sensors for the time spanning mid-2015 to 2018, during which we observed a concentration of swarms as detailed subsequently.

The increase in the detection is consistent across the period studied. Many new detections are related to small events with signals close to the noise floor. However, a significant portion of new detections are the five bursts of small-magnitude (M_L 0.5 – 1.5) swarm-like sequences that double the earthquake rates between November 2016 and May 2017 (Fig. 2a), which we discuss further in the Swarm sequences section. Our catalog has the completeness magnitude (M_c) of 0.5 estimated using the maximum curvature method (Wiemer and Wyss, 2000). Here, we do not use the typical correction factor of 0.2 (Woessner and Wiemer, 2005) because it is advantageous to keep more events for the statistical analysis. The *b*-value slope of the frequency–magnitude distribution is determined to be 0.86 by applying the *b*-Positive method (van der Elst, 2021) to all events with a conservative minimum magnitude difference of 0.2 (Fig. 2b). The *b*-Positive method does not require a complete catalog. With these additional events, the enhanced catalog can unlock new insights into the clustering behaviors of earthquakes in the Groningen gas field.

Clustering behaviors

The nearest-neighbor distance approach is applied to 726 earthquake epicenters in the enhanced catalog with $M_L \geq 0.5$. The distribution of nearest-neighbor distance η_j expanded in the form of rescaled time T_j and rescaled distance R_j is shown in Figure 3a. By fitting η_j with a 1D Gaussian mixture model, we find the best-fit mode separator of $\log_{10} \eta_0 = -3.05$. We find that 522 events (72%) are independent, whereas the remaining 204 events (28%) appear to be clustered (Fig. 3b).

The 2D probability distributions of nearest-neighbor distances of the 100 shuffled catalogs are averaged and shown in Figure 3c. Because the rate of independent events vary only gradually during this period, their distribution similarly concentrates along a line with $\log_{10} T_j + \log_{10} R_j =$ constant with almost all reshuffled events (93%) having $\eta_j \geq \eta_0$, validating the approach and the chosen mode separator. The results are qualitatively similar if the earthquake hypocenters are used instead of the epicenters, accounting also for the depths (Fig. S6). Furthermore, the independent events (those with $\eta_j \geq \eta_0$) have CoV of approximately one, consistent with them being Poissonian. If we were to choose $\eta_0 < -4$, events with $\eta_j \geq \eta_0$ include clusters as CoV becomes significantly greater than one (Fig. S7).

The Schuster spectrum calculated for the nondeclustered catalog shows p-values lower than those expected from a Poisson process starting from periods of about 2–3 days and larger (Fig. S8a). This pattern shows that the catalog contains clusters (Ader and Avouac, 2013), and we can infer they have durations of at least a few days. However, if we use only the independent events, the drifting low p-values disappear (Fig. S8b), further validating the choice of the value of the mode separator chosen.

We proceed to analyze the spatiotemporal evolution of the events from each of the two modes (Fig. 4). The independent events align well with the mapped faults and show a seismicity rate that gradually changes with time. On the other hand, the clustered events show multiple lineations that do not align with the mapped faults and occur as short-duration bursts of events in time. The most prominent clusters are the five bursts of small-magnitude (M_L 0.5–1.5) swarm-like sequences occurring between November 2016 and May 2017 (Fig. 2a). The others appear to be aftershocks of the larger $M_L > 2$ events. By construct, if a sequence has a foreshock, the mainshock will be identified as a clustered event rather than an independent event because the foreshock would be its parent, which explains why some of the larger events are identified as clustered.

The spanning tree created by connecting each event with its nearest neighbor if $\eta_j < \eta_0$ reveals 448 single-event clusters (62% of clustered events) and 73 multievent clusters (38% of clustered events). Their detailed statistics are shown in Figure 5. The average size of the multievent clusters is 3.8 events with a standard deviation of 3.6 events. The large

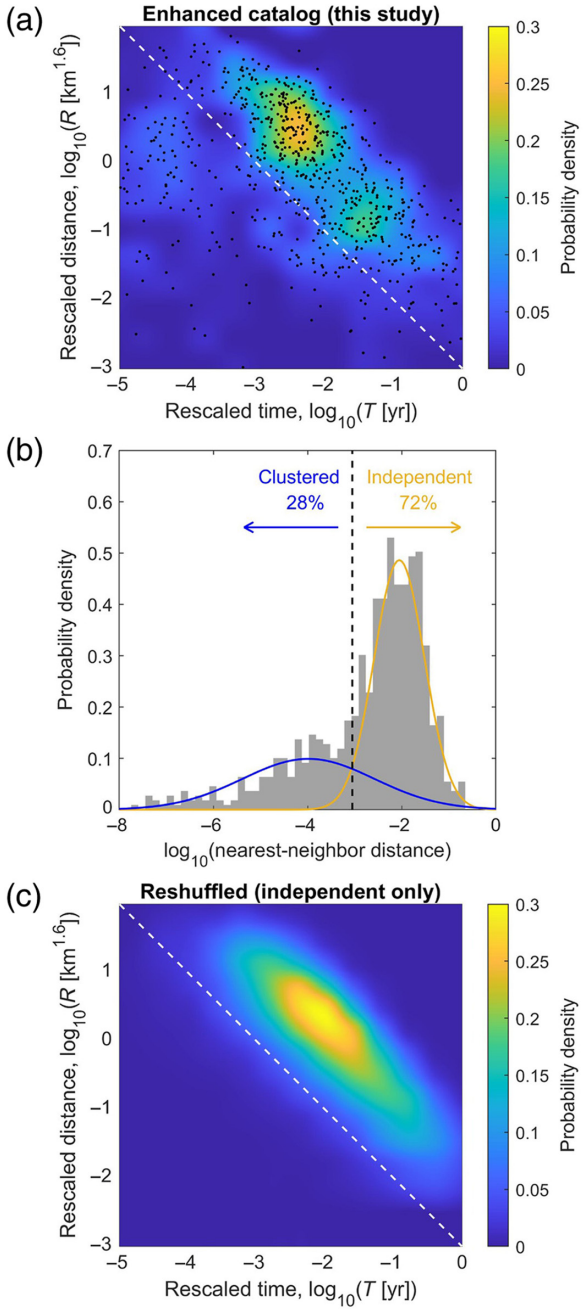

Figure 3. Nearest-neighbor clustering analysis performed on our enhanced seismicity catalog with $M_L \geq 0.5$. Only epicenters are used, and the fractal dimension (d_f) is taken to be 1.6. (a) A joint 2D distribution of the rescaled time and rescaled distance. Each of the black dots represents the proximity of each event to a parent event. (b) Histogram of the nearest-neighbor proximity distance with curves showing the two Gaussian distributions representing the two modes derived from the 1D Gaussian mixture model. (c) The average joint distribution of the rescaled time and rescaled distance derived from 100 catalogs created from reshuffling locations and magnitudes of independent events. The diagonal white dashed lines in panels (a) and (c) and the black vertical dashed line in panel (b) mark the mode separator ($\eta_0 = 10^{-3.05}$) used to perform binary classification of events into either independent or clustered. The color version of this figure is available only in the electronic edition.

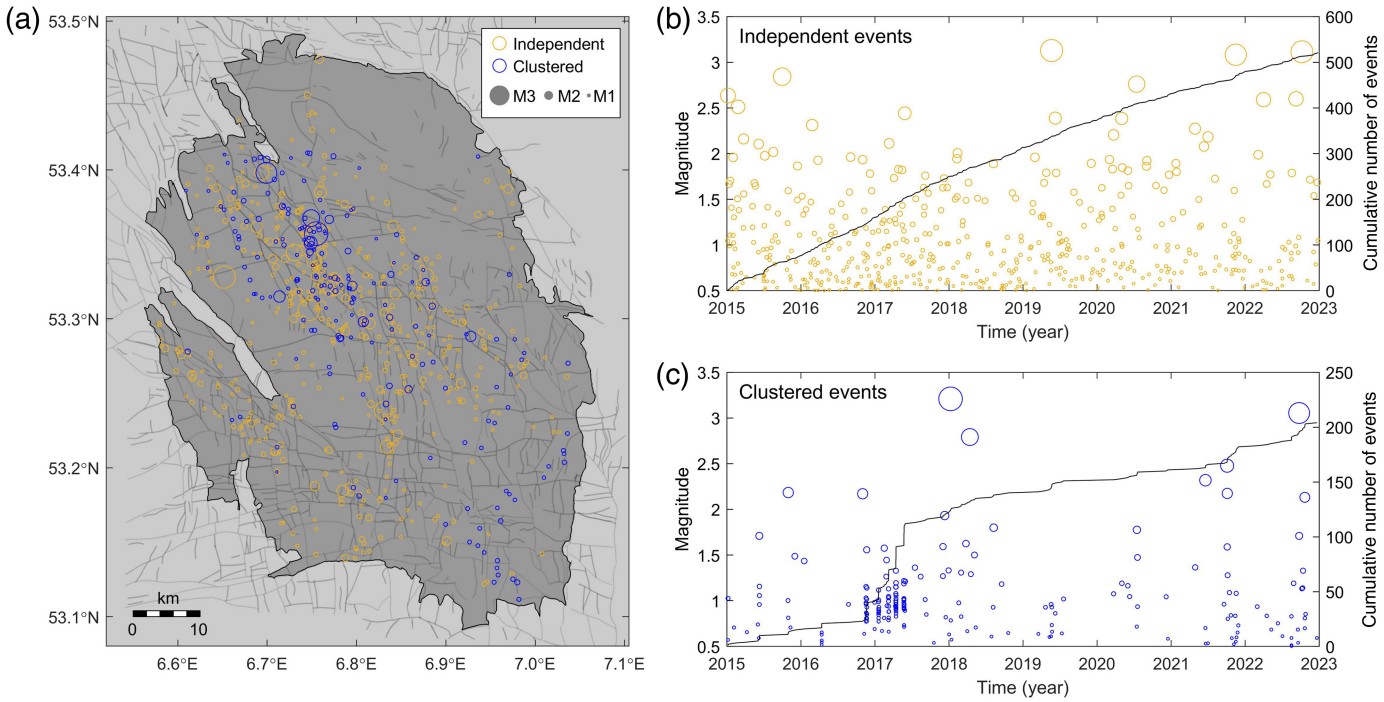

Figure 4. Distribution of independent versus clustered events for $M_L \geq 0.5$ from our enhanced seismicity catalog. (a) Spatial distribution of events color-coded by the mode they belong to. (b) Magnitude and cumulative number of events versus time distribution of the independent events. (c) Same as panel (b) but for clustered events. The color version of this figure is available only in the electronic edition.

standard deviation reflects significant variations in cluster size. All earthquakes with $M_L > 2.5$ are a part of multievent clusters, with the number of events in the cluster growing with mainshock magnitude. On average, the largest aftershock is 1.5 magnitude unit lower than the mainshock, in line with those expected from Båth's law (Richter, 1958). The average leaf depth of these aftershock sequences is 1.3, indicating that most of the events are triggered by the mainshock rather than being aftershocks of aftershocks. On the other end of the spectrum, there are multievent clusters that exist as swarm-like sequences without a clearly identifiable mainshock ($M_{\text{mainshock}} - M_{\text{largest aftershock}} \ll 1$, contradicting Båth's law) and a larger value of average leaf depth (d_{leaf}) of up to 8.7. For an earthquake sequence with an average of two aftershocks for each earthquake, the cluster size (n_{clust}) would then be $2^{d_{\text{leaf}}}$. Therefore, this motivates using d_{leaf} of $\log_2 n_{\text{clust}}$ as a cutoff for binary classification between swarm-like and aftershock-like clusters. Considering only clusters with at least five events, we find seven swarm-like clusters ($d_{\text{leaf}} \geq \log_2 n_{\text{clust}}$) with a total of 77 events (55% of clustered events) and 9 aftershock-like clusters ($d_{\text{leaf}} < \log_2 n_{\text{clust}}$) with a total of 64 events (45% of clustered events). The analysis suggests that the clustered events are slightly dominated by swarm-like sequences. Among aftershock-like clusters, the events are 16% foreshocks, 14% mainshocks, and 70% aftershocks.

Swarm sequences

There were five noticeable swarm-like clusters between November 2016 and May 2017, each lasting 1–5 days and consisting of 10–20 events, with M_L ranging from 0.66 to 1.56 (Fig. 6). Outside of this period, we did not find any other noticeable swarm clusters. Upon further investigation of their kinematics, all swarms migrate with velocities ranging from 3 to 50 km/day. We numbered the swarms from 1 to 5 based on the order that they occurred. The migration occurred along one single direction for swarms 1 and 2 and two different orthogonal directions for swarms 3–5. For swarms 3 and 4, there exist also ~15 hr pauses with no events before the migration direction switches. The migration directions do not follow mapped faults or other known features of the reservoir. Although there are not enough events to determine the exact shape of the migration front, it is possible to model them with $\sqrt{4\pi Dt}$, in which D would be an apparent hydraulic diffusivity and t is the time. In the case of fluid-driven swarms, the fitted D would be related to the hydraulic diffusivity of the fault zones (Shapiro *et al.*, 1997), though with a conversion factor that accounts for the time delays associated with earthquake nucleation (Kim and Avouac, 2023). The swarms in our study have D ranging from 70 to 800 m^2/s, much larger than a commonly accepted range for fluid-driven swarms of 0.005–10 m^2/s (Amezawa *et al.*, 2021). In comparison to other swarms around the world, the scaling between migration velocity and duration places them closer to slow-slip events and swarms driven dominantly by slow-slip events than other

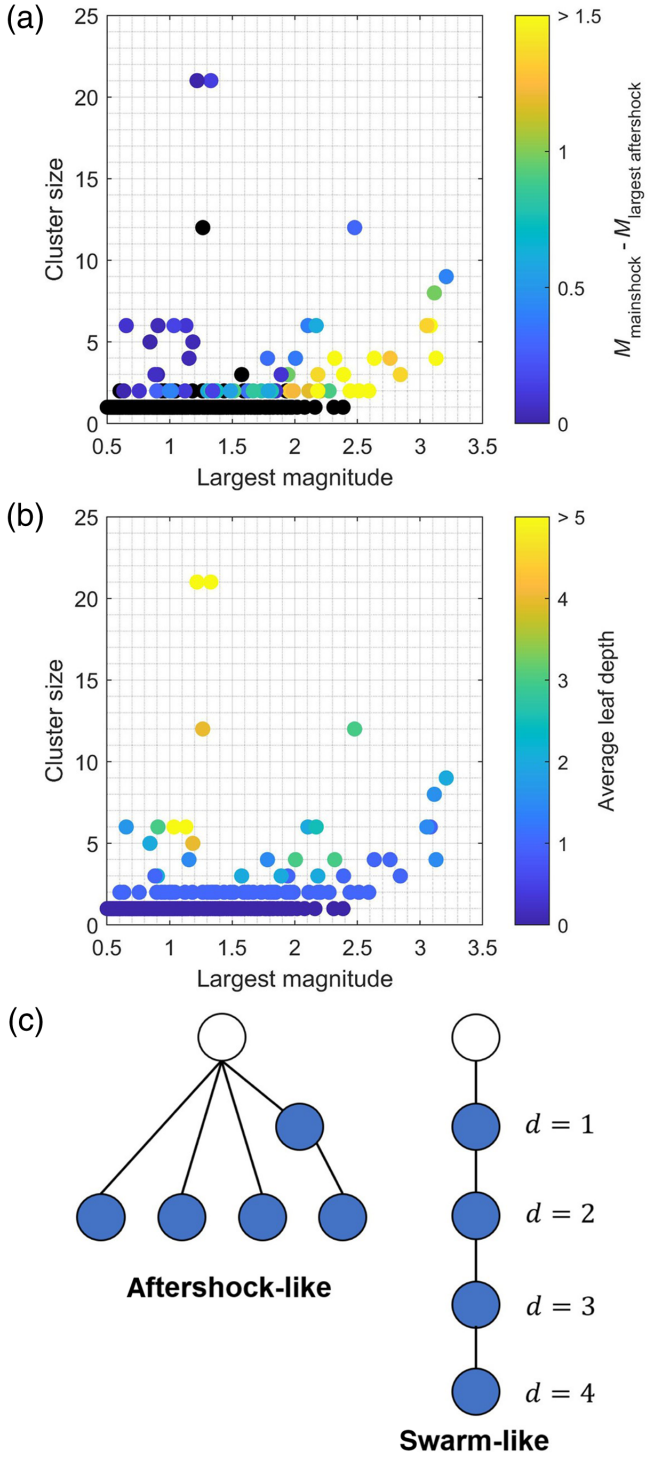

Figure 5. Statistics of the identified clusters. (a) Cluster size (number of events) versus magnitude of the largest event color-coded by the magnitude difference between mainshock and largest aftershock. Black circles denote the case with only one event in the cluster or when the largest earthquake is the last one in the sequence. Panel (b) is the same as (a) but color-coded by the average leaf depth. (c) A schematic showing aftershock-like and swarm-like sequences. The aftershock-like sequence has a smaller average leaf depth than the swarm-like sequence, but each event produces more offspring. The color version of this figure is available only in the electronic edition.

injection-induced swarms (Danré *et al.*, 2022). Fluid may trigger subsequent aseismic slip that expands faster than fluid itself, resulting in much larger apparent diffusivity than the hydraulic diffusivity of the fault zone (Sáez *et al.*, 2022). We further discuss possible drivers for these swarms in the Possible drivers of swarm-like sequences section.

Another interesting observation is that the swarms occurred at a depth of between 1.5 and 2.5 km. While there could be some uncertainty with the absolute depth locations, they are certainly located toward the shallower side when compared to other earthquakes that are generally thought to be located near the top of the reservoir (Willacy *et al.*, 2019; Smith *et al.*, 2020). As a result, this would place them in the 1–2 km thick Zechstein evaporite (salt) above the anhydrite caprock, well above the gas reservoir (Fig. 7).

Discussion

Comparison of clustered fraction with other studies

Induced earthquakes are known to have a lower proportion of clustered events than naturally occurring tectonic earthquakes due to high driving stresses from anthropogenic activities in comparison to tectonic loading (Schoenball *et al.*, 2015; Zaliapin and Ben-Zion, 2016; Cochran *et al.*, 2018; Martínez-Garzón *et al.*, 2018). Here, we compile in Table 1 the clustered proportion of seismicity from different regions as reported by previous studies. We find that the clustered events can account for up to 70% of naturally occurring tectonic earthquakes but no more than 30% of induced earthquakes. The estimate of 28% from this study places the Groningen gas field well within the range estimated for other induced seismicity settings. Other studies on the clustered proportion of seismicity from the Groningen gas field provide different estimates of the clustered proportion varying from a few percent up to 27%, which are generally lower than the 28% that we report here (Candela *et al.*, 2019; Muntendam-Bos, 2020; Post *et al.*, 2021; Trampert *et al.*, 2022). Among those that also use the nearest-neighbor distance approach, Candela *et al.* (2019) found 18% of clustered events between 1993 and 2016, while Muntendam-Bos (2020) finds only 6% of clustered events between 1995 and 2018, but the proportion increases to 22% if consider only the period between 2014 and 2018. On the other hand, Post *et al.* (2021) use the statistics of the interevent times and find a larger value of 27% for the clustered proportion. The scatter of the clustered proportion identified by the different studies can be attributed to various factors, including but not limited to a variation of earthquake rates and clustering behaviors with time (Trugman *et al.*, 2016; Martínez-Garzón *et al.*, 2018; Muntendam-Bos, 2020), the accuracy of earthquake locations (Muntendam-Bos, 2020), and the five swarm sequences occurring between November 2016 and May 2017 that were not previously identified other seismicity catalogs, and the cutoff magnitude employed

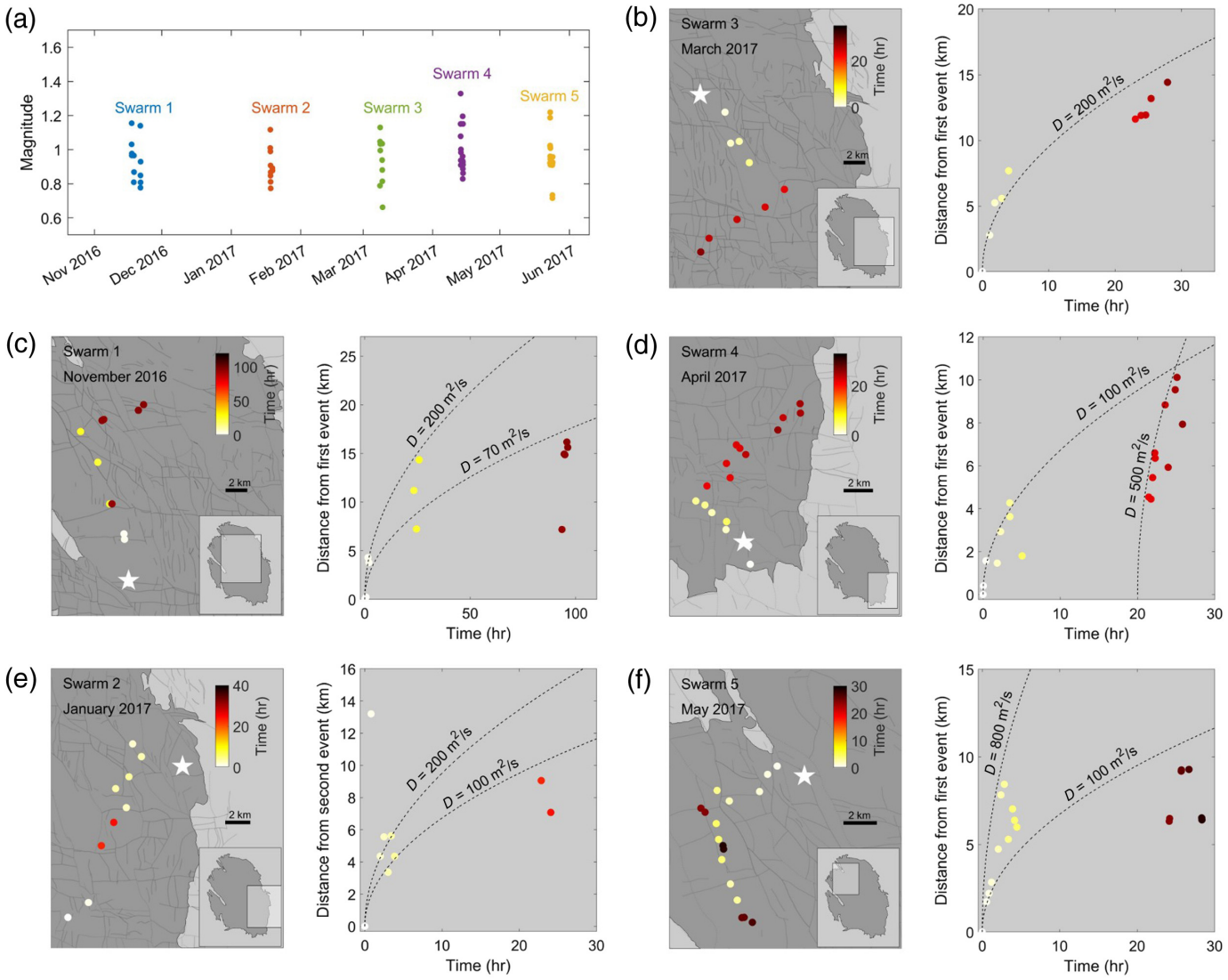

Figure 6. Fast propagating earthquake swarms. (a) Magnitude versus time of the five distinct bursts of swarm-like sequences. Panels (b–f) show the spatiotemporal evolution of these five swarms. The white stars mark the second event in swarm 2 and the first event in all other swarms. The dashed lines show the predicted expansion for the different values of apparent hydraulic diffusivity *D*. The color version of this figure is available only in the electronic edition.

(Zaliapin and Ben-Zion, 2013a). By removing the five swarms, our estimate of the clustered proportion becomes 19%, which is almost equivalent to the estimate from Candela *et al.* (2019). We also calculate the clustered proportion using the different cutoffs and find that the clustered proportion generally decreases with a larger cutoff and becomes stable between 18% and 20% as the cutoff exceeds M_L of 1.2 at which the five swarm sequences are excluded from the analysis (Fig. 8).

Possible drivers of swarm-like sequences

Although the migration of swarms in the Groningen gas field can be modeled with a square root of time typically associated with fluid pressure diffusion (Shapiro *et al.*, 1997), fluid is unlikely to play any dominant role for the following reasons. First, the migration direction should be along the maximum spatial pressure gradient, which follows the spatial derivative of the compaction rate. This contradicts the observations in which the migration direction seems to align more along the contours of constant compaction (Fig. 9a). Second, the migration velocity is on the order of 10 km/day, which requires a much higher hydraulic diffusivity than the values typically expected for fluid-driven swarms (Amezawa *et al.*, 2021). Third, while fault slip can enhance permeability, allowing for faster diffusion rates, the migration directions do not follow mapped faults or any known structures. There may be other unmapped faults that the migration follows because there are focal mechanisms with fault planes not orienting along the mapped faults (Willacy *et al.*, 2019). Nevertheless, because the swarms are located in the Zechstein salt well above the impermeable anhydrite caprock that allows the gas to be preserved for millions of years (Fig. 7), the faults in the Zechstein

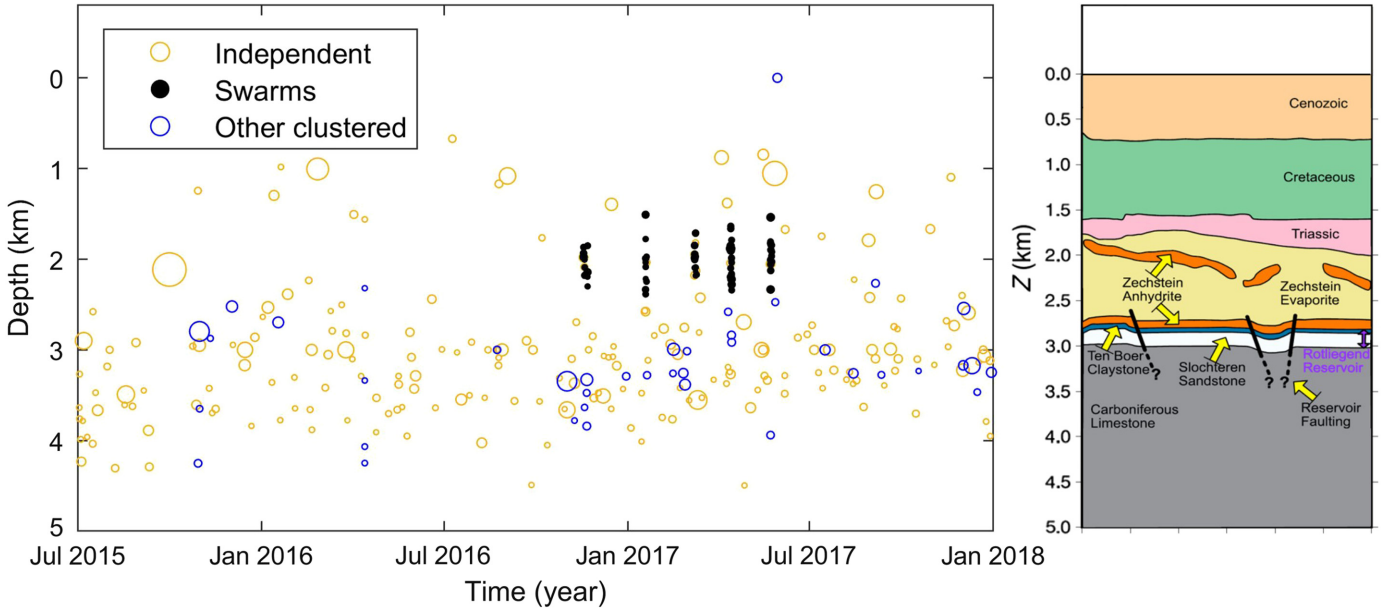

Figure 7. Depth distribution of earthquakes with $M_L \geq 0.5$ from our enhanced seismicity catalog with colors identifying whether they are independent, fast propagating swarms shown in Figure 6, or other clustered events, along with a schematic showing a depth cross-section of the lithologies taken from Smith *et al.* (2019). Only the time period when we have picks from both the surface and borehole sensors is shown. The five swarm sequences are located in the Zechstein evaporite. The color version of this figure is available only in the electronic edition.

layer are probably not hydraulically connected to the reservoir and are most probably located in the anhydrite fragments that are embedded within the Zechstein evaporite rather than in the evaporite itself, which cannot support brittle fractures due to its viscous nature. Hence, the swarms cannot be driven by direct fluid contact.

Besides fluids, cascading earthquakes can create an apparent diffusive expansion front (Helmstetter and Sornette, 2002). However, the swarms consist of only small M_L 0.5–1.5 events, which would correspond to a rupture dimension of ~15–40 m, much smaller than the average distance of ~1 km between events (Fig. 6). Although there could exist a chain of smaller undetectable events that connect the larger ones, this is unlikely as our deep-learning-based workflow should be able to detect some swarm events below M_L 0.5 (Fig. 2); but we detect none. Therefore, cascade triggering is also unlikely.

These swarms occurred just after the period of accelerated compaction (Fig. 9b), suggesting that they might be related to the large strain rate from such a period that could trigger swarms in the Zechstein layer above the reservoir. However, because the compaction rate seems to be more correlated with the rate of independent events rather than the rates of all events (Fig. S9), some additional mechanisms are required to connect compaction to the swarms. Although seismic events in the salt are rare because salt is highly ductile, they can occur in case of large strain rates, for example, related to the collapse of mining cavities (Kinscher *et al.*, 2016) or fault creep (Barnea Cohen *et al.*, 2022), or in relation to fluid injection (Lei *et al.*, 2019). Alternatively, these events could also occur within the anhydrite fragments embedded in the salt (Spetzler and Dost, 2017). Because there are no mining activities in the Zechstein layer and the faults in this layer are most probably not hydraulically connected to the reservoir, propagating episodes of aseismic deformation are the most probable mechanisms. Although there are no detectable geodetic signals in either the GPS, InSAR, or the fiber-optic borehole strains (Oates *et al.*, 2022) during the time of the swarms, aseismic creep may be located too deep or too small to be detected. Swarms that are driven by aseismic slip generally propagate at high velocity in the order of kilometers per hour (Lohman and McGuire, 2007; Sirorattanakul *et al.*, 2022) and can have a square root of time migration (Sáez *et al.*, 2022), which is consistent with the observations of the Groningen swarms. The aseismic fault creep could occur within the fragments of anhydrite embedded in the Zechstein evaporite. Such creep can be driven by the long-range poroelastic stress changes incurred by pore-pressure changes in the reservoir. Poroelastic effects are indeed needed to explain both the surface subsidence and the induced seismicity at Groningen and are therefore explicitly included in most models (Bourne *et al.*, 2014; Buijze *et al.*, 2017; Dempsey and Suckale, 2017; Candela *et al.*, 2019; Smith *et al.*, 2022). Alternatively, aseismic fault creep may be driven by stress induced by bulk creep in the surrounding Zechstein evaporite as the salt redistributes, possibly in response to the disturbances from the historic gas production. Because these swarms are not driven directly by stress changes from the industrial operations, they are not yet accounted for in induced seismicity forecasting models for the Groningen gas field.

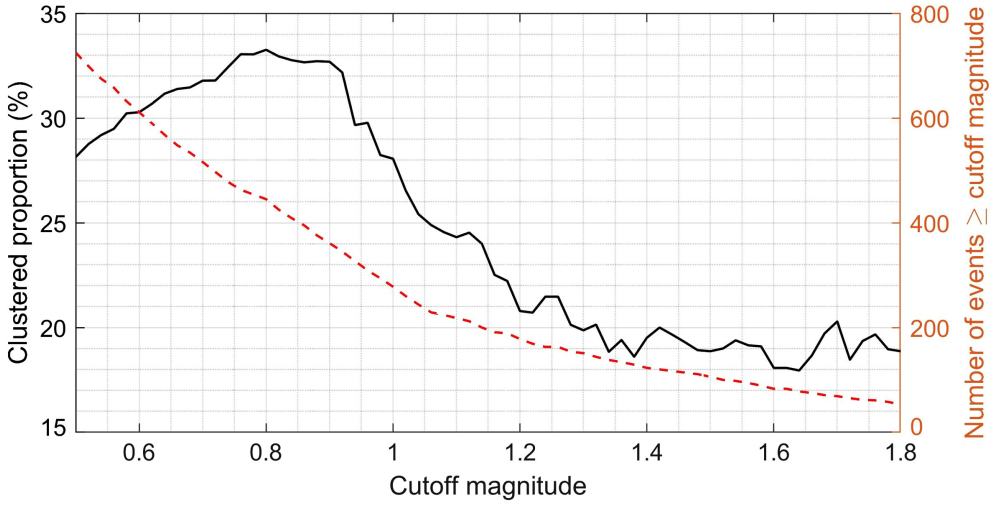

Figure 8. Variations of the clustered proportion for the different cutoff magnitude. The dashed line shows the number of events larger than or equal to a given cutoff magnitude. The color version of this figure is available only in the electronic edition.

Conclusions

By applying a deep-learning-based workflow for earthquake detection to seismic data from the Groningen gas field, we identify and locate a total of 1369 events from 2015 to 2022, almost two times more than the standard KNMI catalog. Despite being automatically generated products, the locations and magnitudes of the overlapping events display a high degree of similarity with the KNMI catalog. Analysis of the nearest-neighbor distance reveals that the clusters account for 28% of all events. Among the clustered events, approximately half are swarm-like clusters, whereas the remaining half are aftershock-like clusters. The swarm-like clusters include five distinct swarm sequences that migrate at remarkably fast velocities between 3 and 50 km/day along directions that do not follow mapped faults or existing structures and frequently exhibit a sharp turn in the middle of the sequence. Based on the observations of fast velocities and their depths in the Zechstein salt above the reservoir caprock, the swarms are most likely not driven by fluids but

TABLE 1
A Compilation of Clustered Fraction of Seismicity from Different Regions

Region	Type of Seismicity	Magnitude Cutoff	Clustered Fraction
Southern California (Zaliapin and Ben-Zion, 2013a)	Mostly tectonic	2	0.70
San Jacinto fault zone, California, United States (Zaliapin and Ben-Zion, 2016)	Tectonic	1	0.34
Coso geothermal field, California, United States (Zaliapin and Ben-Zion, 2016)	Mixed	1	0.44
Salton Sea geothermal field, California, United States (Zaliapin and Ben-Zion, 2016)	Mixed	1.5	0.69
Geysers geothermal field, California, United States (Zaliapin and Ben-Zion, 2016)	Induced	1.0	0.17
TauTona gold mine, South Africa (Zaliapin and Ben-Zion, 2016)	Induced	1.5	0.12
Saltwater disposal, Oklahoma (Cochran *et al.*, 2020)	Induced	0.95	0.30
Hydraulic fracturing in western Alberta, Canada (Karimi and Davidsen, 2023)	Induced	0.2	0.25
Groningen gas field, Netherlands, KNMI catalog (Candela *et al.*, 2019)	Induced	1.0	0.18
Groningen gas field, Netherlands, KNMI catalog (Post *et al.*, 2021)	Induced	1.3	0.27
Groningen gas field, Netherlands, KNMI catalog between January 1995 and January 2019 (Muntendam-Bos, 2020)	Induced	1.2	0.06
Groningen gas field, Netherlands, KNMI catalog between May 2014 and January 2019 (Muntendam-Bos, 2020)	Induced	1.2	0.22
Groningen gas field, Netherlands, enhanced catalog (this study)	Induced	0.5	0.28
Groningen gas field, Netherlands, enhanced catalog (this study)	Induced	1.2	0.21

With the exception of Post *et al.* (2021), which utilizes the statistics of interevent times, all other studies utilized the nearest-neighbor distance approach (Zaliapin *et al.*, 2008; Zaliapin and Ben-Zion, 2013a). KNMI, Royal Netherlands Meteorological Institute.

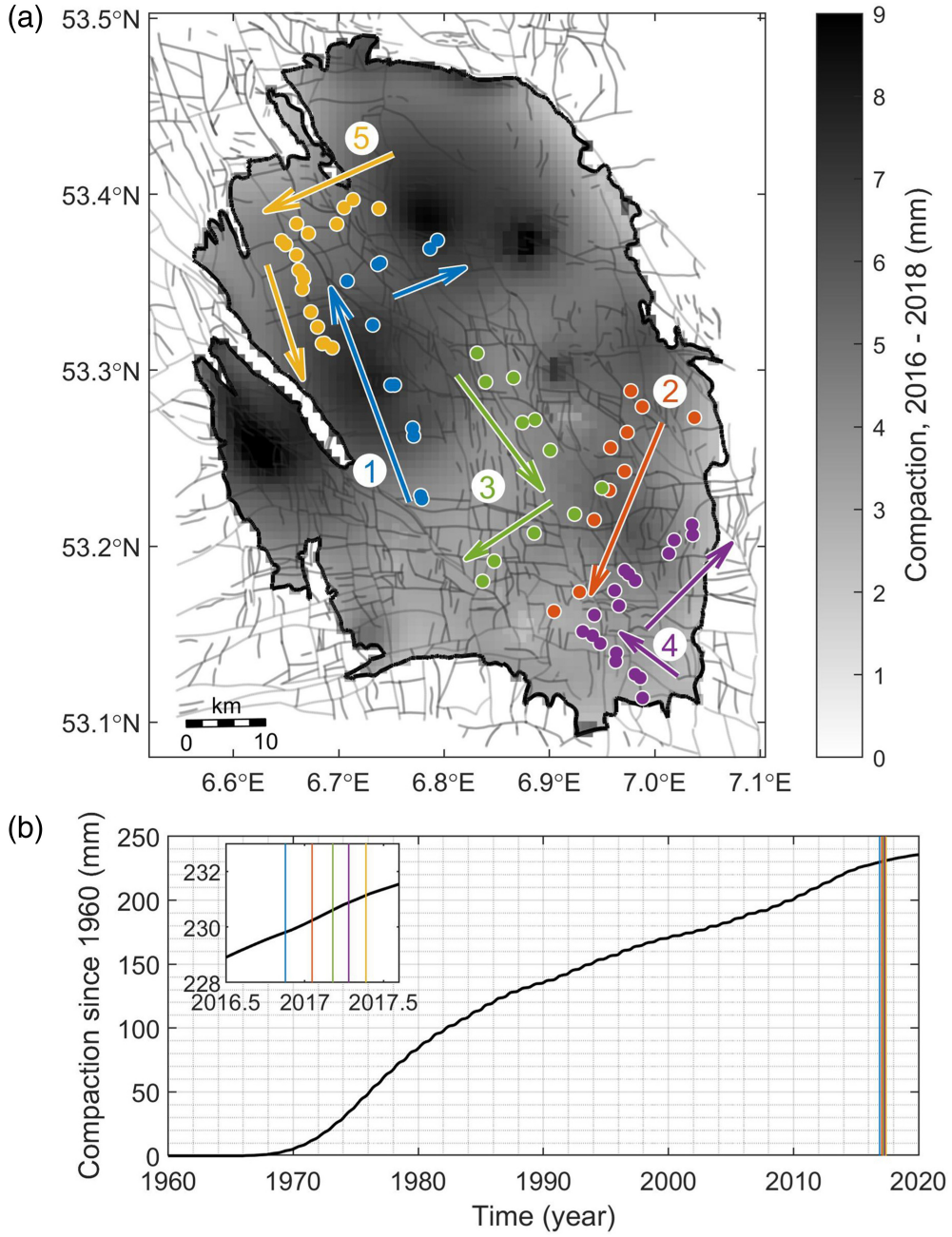

Figure 9. Comparison of the swarms with reservoir compaction. (a) Spatial distribution of modeled reservoir compaction between 2016 and 2018. The calculation is done using a simple expression $C = C_m \times \Delta P \times h$ relating compaction C with the compressibility C_m from Smith *et al.* (2019) constrained with geodetic data, pressure depletion ΔP from Acosta *et al.* (2023) calculated using a simplified reservoir model from Meyer *et al.* (2023) constrained with pressure measurements from the borehole sensors, and the reservoir thickness h. The circles with different colors denote the five different swarms shown in Figure 6. (b) Average compaction in the reservoir versus time. The vertical lines denote the timing of the five swarms. The inset shows a zoomed-in during the time of swarms. The color version of this figure is available only in the electronic edition.

rather by other aseismic processes such as propagating aseismic creep. The magnitude of these swarms is within the detectable range of the KNMI catalog, but they were not previously identified and reported. With a better catalog, we can enhance our understanding of the mechanics of earthquake clusters and allow us to better incorporate their contributions to seismic hazards into induced seismicity forecasting models and their associated uncertainties (Kaveh *et al.*, 2023).

Data and Resources

Raw seismic waveforms were accessed through the Observatories and Research Facilities for European Seismology (ORFEUS) International Federation of Digital Seismograph Networks (FDSN) client via a Python script using the package ObsPy (https://docs.obspy.org/; Beyreuther *et al.*, 2010). The 3D seismic velocity and faults map were provided to us by Shell Global Solutions International B.V. Computer programs used to generate the enhanced seismicity catalog are previously published and can be found in the following references: seismic phase detection software PhaseNet (https://github.com/AI4EPS/PhaseNet; Zhu and Beroza, 2019), seismic phase association software GaMMA (https://github.com/AI4EPS/GaMMA; Zhu *et al.*, 2022), hypocenter inversion software HypoSVI (https://github.com/Ulvetanna/HypoSVI; Smith *et al.*, 2021). The seismicity catalog from the Royal Netherland Meteorological Survey (KNMI) is available online at www.knmi.nl. MATLAB version 2020a was used to analyze data and prepare figures. The enhanced seismicity catalog generated in this study along with the picks of arrival times can be found in the supplemental material. Codes used for data analysis and figure generation are made available online through CaltechDATA repository at https://data.caltech.edu/records/emasj-np244. All websites were last accessed in March 2024. The supplemental material for this article includes supplemental figures, enhanced high-resolution seismicity catalog (data S1), and the associated picks of *P*- and *S*-wave arrival times (data S2).

Declaration of Competing Interests

The authors acknowledge that there are no conflicts of interest recorded.

Acknowledgments

This research is supported by the National Science Foundation (NSF)/Industry-University Collaborative Research Center "Geomechanics and Mitigation of Geohazards" (NSF Award Number 1822214), and the Enhancement Project GMG-3 funded by Nederlandse Aardolie Maatschappij (NAM). The authors gratefully acknowledge data and support from Shell Global Solutions and thank Editor-in-Chief Allison Bent, the associate editor, and two anonymous reviewers for insightful and detailed comments, which greatly improved the quality of the article.

References

Acosta, M., J. Avouac, J. D. Smith, K. Sirorattanakul, H. Kaveh, and S. J. Bourne (2023). Earthquake nucleation characteristics revealed by seismicity response to seasonal stress variations induced by gas production at Groningen, *Geophys. Res. Lett.* **50,** no. 19, e2023GL105455, doi: 10.1029/2023GL105455.

Ader, T. J., and J.-P. Avouac (2013). Detecting periodicities and declustering in earthquake catalogs using the Schuster spectrum, application to Himalayan seismicity, *Earth Planet. Sci. Lett.* **377/378,** 97–105, doi: 10.1016/j.epsl.2013.06.032.

Ake, J., K. Mahrer, D. O'Connell, and L. Block (2005). Deep-injection and closely monitored induced seismicity at Paradox Valley, Colorado, *Bull. Seismol. Soc. Am.* **95,** no. 2, 664–683, doi: 10.1785/0120040072.

Albaric, J., V. Oye, N. Langet, M. Hasting, I. Lecomte, K. Iranpour, M. Messeiller, and P. Reid (2014). Monitoring of induced seismicity during the first geothermal reservoir stimulation at Paralana, Australia, *Geothermics* **52,** 120–131, doi: 10.1016/j.geothermics.2013.10.013.

Amezawa, Y., T. Maeda, and M. Kosuga (2021). Migration diffusivity as a controlling factor in the duration of earthquake swarms, *Earth Planets Space* **73,** no. 1, 148, doi: 10.1186/s40623-021-01480-7.

Atkinson, G. M., D. W. Eaton, and N. Igonin (2020). Developments in understanding seismicity triggered by hydraulic fracturing, *Nat. Rev. Earth Environ.* **1,** no. 5, 264–277, doi: 10.1038/s43017-020-0049-7.

Audin, L., J.-P. Avouac, M. Flouzat, and J.-L. Plantet (2002). Fluid-driven seismicity in a stable tectonic context: The Remiremont fault zone, Vosges, France, *Geophys. Res. Lett.* **29,** no. 6, 13-1–13–4, doi: 10.1029/2001GL012988.

Baiesi, M., and M. Paczuski (2004). Scale-free networks of earthquakes and aftershocks, *Phys. Rev. E* **69,** no. 6, 066106, doi: 10.1103/PhysRevE.69.066106.

Baisch, S., R. Weidler, R. Voros, D. Wyborn, and L. De Graaf (2006). Induced seismicity during the stimulation of a Geothermal HFR Reservoir in the Cooper Basin, Australia, *Bull. Seismol. Soc. Am.* **96,** no. 6, 2242–2256, doi: 10.1785/0120050255.

Barnea Cohen, O., S. Cesca, T. Dahm, A. Hofstetter, Y. Hamiel, and A. Agnon (2022). Seismicity induced at the Northern Dead Sea Transform Fault, Kinneret (Sea of Galilee) basin, by shallow creep Involving a salt body, *Tectonics* **41,** no. 10, e2022TC007247, doi: 10.1029/2022TC007247.

Beyreuther, M., R. Barsch, L. Krischer, T. Megies, Y. Behr, and J. Wassermann (2010). ObsPy: A Python toolbox for seismology, *Seismol. Res. Lett.* **81,** no. 3, 530–533, doi: 10.1785/gssrl.81.3.530.

Bourne, S. J., and S. J. Oates (2017). Extreme threshold failures within a heterogeneous elastic thin sheet and the spatial-temporal development of Induced seismicity within the Groningen gas field, *J. Geophys. Res.* **122,** no. 12, 10,299–10,320, doi: 10.1002/2017JB014356.

Bourne, S. J., S. J. Oates, and J. van Elk (2018). The exponential rise of induced seismicity with increasing stress levels in the Groningen gas field and its implications for controlling seismic risk, *Geophys. J. Int.* **213,** no. 3, 1693–1700, doi: 10.1093/gji/ggy084.

Bourne, S. J., S. J. Oates, J. Van Elk, and D. Doornhof (2014). A seismological model for earthquakes induced by fluid extraction from a subsurface reservoir, *J. Geophys. Res.* **119,** no. 12, 8991–9015, doi: 10.1002/2014JB011663.

Buijze, L., P. A. J. Van Den Bogert, B. B. T. Wassing, B. Orlic, and J. Ten Veen (2017). Fault reactivation mechanisms and dynamic rupture modelling of depletion-induced seismic events in a Rotliegend gas reservoir, *Neth. J. Geosci.* **96,** no. 5, s131–s148, doi: 10.1017/njg.2017.27.

Burkitov, U., H. Van Oeveren, and P. Valvatne (2016). Groningen field review 2015 subsurface dynamic modelling report, Nederlandse Aardolie Maatschappij, available at https://nam-feitenencijfers.data-app.nl/download/rapport/e683753a-e085-417d-995d-b7ae7a9c820f?open=true (last accessed March 2024).

Candela, T., S. Osinga, J. Ampuero, B. Wassing, M. Pluymaekers, P. A. Fokker, J. Wees, H. A. Waal, and A. G. Muntendam-Bos (2019). Depletion-induced seismicity at the Groningen gas field: Coulomb rate-and-state models including differential compaction effect, *J. Geophys. Res.* **124,** no. 7, 7081–7104, doi: 10.1029/2018JB016670.

Candela, T., M. Pluymaekers, J.-P. Ampuero, J.-D. van Wees, L. Buijze, B. Wassing, S. Osinga, N. Grobbe, and A. G. Muntendam-Bos (2022). Controls on the spatio-temporal patterns of induced seismicity in Groningen constrained by physics-based modelling with Ensemble-Smoother data assimilation, *Geophys. J. Int.* **229,** no. 2, 1282–1308, doi: 10.1093/gji/ggab497.

Chen, X., and P. M. Shearer (2011). Comprehensive analysis of earthquake source spectra and swarms in the Salton Trough, California, *J. Geophys. Res.* **116,** no. B9, doi: 10.1029/2011JB008263.

Clayton, P., G. Zalachoris, E. Rathje, T. Bheemasetti, S. Caballero, X. Yu, and S. Bennett (2016). The geotechnical aspects of the September 3, 2016 M 5.8 Pawnee, Oklahoma earthquake, *G69885*, GEER Association, Berkeley, California, 1–14.

Cochran, E. S., Z. E. Ross, R. M. Harrington, S. L. Dougherty, and J. L. Rubinstein (2018). Induced earthquake families reveal distinctive evolutionary patterns near disposal wells, *J. Geophys. Res.* **123,** no. 9, 8045–8055, doi: 10.1029/2018JB016270.

Cochran, E. S., A. Wickham-Piotrowski, K. B. Kemna, R. M. Harrington, S. L. Dougherty, and A. F. Peña Castro (2020). Minimal clustering of injection-induced earthquakes observed with a large-n seismic array, *Bull. Seismol. Soc. Am.* **110,** no. 5, 2005–2017, doi: 10.1785/0120200101.

Dahm, T., and S. Hainzl (2022). A Coulomb stress response model for time-dependent earthquake forecasts, *J. Geophys. Res.* **127,** no. 9, e2022JB024443, doi: 10.1029/2022JB024443.

Danré, P., L. De Barros, F. Cappa, and J. Ampuero (2022). Prevalence of aseismic slip linking fluid injection to natural and anthropogenic seismic swarms, *J. Geophys. Res.* **127,** no. 12, e2022JB025571, doi: 10.1029/2022JB025571.

de Jager, J., and C. Visser (2017). Geology of the Groningen field—An overview, *Neth. J. Geosci.* **96,** no. 5, s3–s15, doi: 10.1017/njg.2017.22.

de Waal, J. A., A. G. Muntendam-Bos, and J. P. A. Roest (2015). Production induced subsidence and seismicity in the Groningen gas field—Can it be managed? *Proc. Int. Assoc. Hydrol. Sci.* **372,** 129–139, doi: 10.5194/piahs-372-129-2015.

Dempsey, D., and J. Suckale (2017). Physics-based forecasting of induced seismicity at Groningen gas field, the Netherlands, *Geophys. Res. Lett.* **44,** no. 15, 7773–7782, doi: 10.1002/2017GL073878.

Dost, B., B. Edwards, and J. J. Bommer (2018). The relationship between M and ML: A review and application to induced seismicity in the Groningen gas field, the Netherlands, *Seismol. Res. Lett.* **89,** no. 3, 1062–1074, doi: 10.1785/02201700247.

Dost, B., E. Ruigrok, and J. Spetzler (2017). Development of seismicity and probabilistic hazard assessment for the Groningen gas field, *Neth. J. Geosci.* **96,** no. 5, s235–s245, doi: 10.1017/njg.2017.20.

Dublanchet, P., and L. De Barros (2021). Dual seismic migration velocities in seismic swarms, *Geophys. Res. Lett.* **48,** no. 1, doi: 10.1029/2020GL090025.

Ellsworth, W. L. (2013). Injection-induced earthquakes, *Science* **341,** no. 6142, 1225942, doi: 10.1126/science.1225942.

Goebel, T. H. W., M. Weingarten, X. Chen, J. Haffener, and E. E. Brodsky (2017). The 2016 Mw5.1 Fairview, Oklahoma earthquakes: Evidence for long-range poroelastic triggering at >40 km from fluid disposal wells, *Earth Planet. Sci. Lett.* **472,** 50–61, doi: 10.1016/j.epsl.2017.05.011.

Grigoli, F., S. Cesca, E. Priolo, A. P. Rinaldi, J. F. Clinton, T. A. Stabile, B. Dost, M. G. Fernandez, S. Wiemer, and T. Dahm (2017). Current challenges in monitoring, discrimination, and management of induced seismicity related to underground industrial activities: A European perspective, *Rev. Geophys.* **55,** no. 2, 310–340, doi: 10.1002/2016RG000542.

Gualandi, A., C. Nichele, E. Serpelloni, L. Chiaraluce, L. Anderlini, D. Latorre, M. E. Belardinelli, and J.-P. Avouac (2017). Aseismic deformation associated with an earthquake swarm in the northern Apennines (Italy), *Geophys. Res. Lett.* **44,** no. 15, 7706–7714, doi: 10.1002/2017GL073687.

Hainzl, S., and T. Fischer (2002). Indications for a successively triggered rupture growth underlying the 2000 earthquake swarm in Vogtland/NW Bohemia, *J. Geophys. Res.* **107,** no. B12, ESE 5-1–ESE 5-9, doi: 10.1029/2002JB001865.

Heimisson, E. R., J. D. Smith, J.-P. Avouac, and S. J. Bourne (2022). Coulomb threshold rate-and-state model for fault reactivation: Application to induced seismicity at Groningen, *Geophys. J. Int.* **228,** no. 3, 2061–2072, doi: 10.1093/gji/ggab467.

Helmstetter, A., and D. Sornette (2002). Diffusion of epicenters of earthquake aftershocks, Omori's law, and generalized continuous-time random walk models, *Phys. Rev. E* **66,** no. 6, 061104, doi: 10.1103/PhysRevE.66.061104.

Hicks, A. (2011). Clustering in multidimensional spaces with applications to statistical analysis of earthquake clustering, University of Nevada, Reno, Nevada.

Hough, S. E. (2015). Shaking intensity from injection-induced versus tectonic earthquakes in the central-eastern United States, *The Leading Edge* **34,** no. 6, 690–697.

Hubbert, M. K., and W. W. Rubey (1959). Role of fluid pressure in mechanics of overthrust faulting, *Geol. Soc. Am. Bull.* **70,** 115–166.

Jiang, Y., S. V. Samsonov, and P. J. González (2022). Aseismic fault slip during a shallow normal-faulting seismic swarm constrained using a physically informed geodetic inversion method, *J. Geophys. Res.* **127,** no. 7, e2021JB022621, doi: 10.1029/2021JB022621.

Karimi, K., and J. Davidsen (2023). Separating primary and secondary mechanisms for seismicity induced by hydraulic fracturing, *Bull. Seismol. Soc. Am.* **113,** no. 5, 1982–1991, doi: 10.1785/0120220200.

Kaveh, H., P. Batlle, M. Acosta, P. Kulkarni, S. J. Bourne, and J. P. Avouac (2023). Induced seismicity forecasting with uncertainty quantification: Application to the Groningen gas field, *Seismol. Res. Lett.* **95,** no. 2A, 773–790, doi: 10.1785/0220230179.

Keranen, K. M., and M. Weingarten (2018). Induced seismicity, *Annu. Rev. Earth Planet. Sci.* **46,** 149–174, doi: 10.1146/annurev-earth-082517-010054.

Kim, T., and J. Avouac (2023). Stress-based and convolutional forecasting of injection-induced seismicity: Application to the Otaniemi geothermal reservoir stimulation, *J. Geophys. Res.* **128,** no. 4, e2022JB024960, doi: 10.1029/2022JB024960.

Kinscher, J., S. Cesca, P. Bernard, I. Contrucci, A. Mangeney, J. P. Piguet, and P. Bigarré (2016). Resolving source mechanisms of microseismic swarms induced by solution mining, *Geophys. J. Int.* **206,** no. 1, 696–715, doi: 10.1093/gji/ggw163.

Kühn, D., S. Hainzl, T. Dahm, G. Richter, and I. Vera Rodriguez (2022). A review of source models to further the understanding of the seismicity of the Groningen field, *Neth. J. Geosci.* **101,** e11, doi: 10.1017/njg.2022.7.

Kwiatek, G., T. Saarno, T. Ader, F. Bluemle, M. Bohnhoff, M. Chendorain, G. Dresen, P. Heikkinen, I. Kukkonen, P. Leary, *et al.* (2019). Controlling fluid-induced seismicity during a 6.1-km-deep geothermal stimulation in Finland, *Sci. Adv.* **5,** no. 5, eaav7224, doi: 10.1126/sciadv.aav7224.

Langenbruch, C., M. Weingarten, and M. D. Zoback (2018). Physics-based forecasting of man-made earthquake hazards in Oklahoma and Kansas, *Nat. Commun.* **9,** 3946, doi: 10.1038/s41467-018-06167-4.

Lei, X., Z. Wang, and J. Su (2019). Possible link between long-term and short-term water injections and earthquakes in salt mine and shale gas site in Changning, south Sichuan Basin, China, *Earth Planet. Phys.* **3,** no. 6, 510–525, doi: 10.26464/epp2019052.

Lohman, R. B., and J. J. McGuire (2007). Earthquake swarms driven by aseismic creep in the Salton Trough, California, *J. Geophys. Res.* **112,** no. B4, doi: 10.1029/2006JB004596.

Luu, K., M. Schoenball, C. M. Oldenburg, and J. Rutqvist (2022). Coupled hydromechanical modeling of induced seismicity from CO_2 injection in the Illinois basin, *J. Geophys. Res.* **127,** no. 5, e2021JB023496, doi: 10.1029/2021JB023496.

Martínez-Garzón, P., I. Zaliapin, Y. Ben-Zion, G. Kwiatek, and M. Bohnhoff (2018). Comparative study of earthquake clustering in relation to hydraulic activities at geothermal fields in California, *J. Geophys. Res.* **123,** 4041–4062, doi: 10.1029/2017JB014972.

Meyer, H., J. D. Smith, S. Bourne, and J.-P. Avouac (2023). *An Integrated Framework for Surface Deformation Modelling and*

Induced Seismicity Forecasting Due to Reservoir Operations, Vol. 528, Geological Society, London, United Kingdom, Special Publications, 299–318, doi: 10.1144/SP528-2022-169.

Moein, M. J. A., C. Langenbruch, R. Schultz, F. Grigoli, W. L. Ellsworth, R. Wang, A. P. Rinaldi, and S. Shapiro (2023). The physical mechanisms of induced earthquakes, *Nat. Rev. Earth Environ.* **4,** no. 12, 847–863, doi: 10.1038/s43017-023-00497-8.

Mogi, K. (1963). Some discussions on aftershocks, foreshocks and earthquake swarms—The fracture of a semi-infinite body caused by an inner stress origin and its relation to the earthquake phenomena (3rd paper), *Bull. Earthq. Res. Inst. Univ. Tokyo* **41,** no. 3, 615–658.

Muntendam-Bos, A. G. (2020). Clustering characteristics of gas-extraction induced seismicity in the Groningen gas field, *Geophys. J. Int.* **221,** no. 2, 879–892, doi: 10.1093/gji/ggaa038.

Muntendam-Bos, A. G., J. P. A. Roest, and H. A. De Waal (2017). The effect of imposed production measures on gas extraction induced seismic risk, *Neth. J. Geosci.* **96,** no. 5, s271–s278, doi: 10.1017/njg.2017.29.

Nederlandse Aardolie Maatschappij (2017). Groningen Velocity Model 2017, Groningen full elastic velocity model September 2017.

NORSAR (2018). Review of the public KNM induced earthquake catalogue from the Groningen gas field, Project Phase 1, WP1, available at https://kemprogramma.nl/file/download/18f4a605-4bbc-401a-b68e-8bd840b3d05b/1562832346kem11%20norsar_sodm_groningenreview_wp1.pdf (last accessed March 2024).

Nur, A., and J. R. Booker (1972). Aftershocks caused by pore fluid flow? *Science* **175,** no. 4024, 885–887, doi: 10.1126/science.175.4024.885.

Oates, S., A. J. Landman, O. van der Wal, H. Baehr, and H. Piening (2022). Geomechanical, seismological, and geodetic data pertaining to the Groningen gas field: A data package used in the "Mmax II Workshop", on constraining the maximum earthquake magnitude in the Groningen field, Utrecht University, doi: 10.24416/UU01-RHHRPY.

Ogata, Y. (1988). Statistical models for earthquake occurrences and residual analysis for point processes, *J. Am. Stat. Assoc.* **83,** no. 401, 9–27.

Omori, F. (1894). On the aftershocks of earthquakes, *J. Coll. Sci. Imp. Univ. Tokyo* **7,** 111–200.

Park, Y., S. M. Mousavi, W. Zhu, W. L. Ellsworth, and G. C. Beroza (2020). Machine-learning-based analysis of the Guy-Greenbrier, Arkansas earthquakes: A tale of two sequences, *Geophys. Res. Lett.* **47,** no. 6, e2020GL087032, doi: 10.1029/2020GL087032.

Passarelli, L., S. Hainzl, S. Cesca, F. Maccaferri, M. Mucciarelli, D. Roessler, F. Corbi, T. Dahm, and E. Rivalta (2015). Aseismic transient driving the swarm-like seismic sequence in the Pollino range, Southern Italy, *Geophys. J. Int.* **201,** no. 3, 1553–1567, doi: 10.1093/gji/ggv111.

Post, R. A. J., M. A. J. Michels, J.-P. Ampuero, T. Candela, P. A. Fokker, J.-D. Van Wees, R. W. V. D. Hofstad, and E. R. V. D. Heuvel (2021). Interevent-time distribution and aftershock frequency in non-stationary induced seismicity, *Sci. Rep.* **11,** no. 1, 3540, doi: 10.1038/s41598-021-82803-2.

Richter, C. (1958). *Elementary Seismology*, W. H. Freeman and Co, San Francisco, California.

Richter, G., S. Hainzl, T. Dahm, and G. Zöller (2020). Stress-based, statistical modeling of the induced seismicity at the Groningen gas field, The Netherlands, *Environ. Earth Sci.* **79,** no. 11, 252, doi: 10.1007/s12665-020-08941-4.

Ross, Z. E., and E. S. Cochran (2021). Evidence for latent crustal fluid injection transients in Southern California from long-duration earthquake swarms, *Geophys. Res. Lett.* **48,** no. 12, doi: 10.1029/2021GL092465.

Ruhl, C. J., R. E. Abercrombie, K. D. Smith, and I. Zaliapin (2016). Complex spatiotemporal evolution of the 2008 M_w 4.9 Mogul earthquake swarm (Reno, Nevada): Interplay of fluid and faulting, *J. Geophys. Res.* **121,** no. 11, 8196–8216, doi: 10.1002/2016JB013399.

Sáez, A., B. Lecampion, P. Bhattacharya, and R. C. Viesca (2022). Three-dimensional fluid-driven stable frictional ruptures, *J. Mech. Phys. Solids* **160,** 104754, doi: 10.1016/j.jmps.2021.104754.

Schoenball, M., N. C. Davatzes, and J. M. G. Glen (2015). Differentiating induced and natural seismicity using space-time-magnitude statistics applied to the Coso Geothermal field, *Geophys. Res. Lett.* **42,** no. 15, 6221–6228, doi: 10.1002/2015GL064772.

Schuster, A. (1897). On lunar and solar periodicities of earthquakes, *Proc. Math. Phys. Sci.* **61,** 455–465.

Segall, P. (1989). Earthquakes triggered by fluid extraction, *Geology* **17,** 942–946.

Segall, P., and S. Lu (2015). Injection-induced seismicity: Poroelastic and earthquake nucleation effects, *J. Geophys. Res.* **120,** no. 7, 5082–5103, doi: 10.1002/2015JB012060.

Segall, P., J. Grasso, and A. Mossop (1994). Poroelastic stressing and induced seismicity near the Lacq gas field, southwestern France, *J. Geophys. Res.* **99,** no. B8, 15,423–15,438, doi: 10.1029/94JB00989.

Shapiro, S. A., E. Huenges, and G. Borm (1997). Estimating the crust permeability from fluid-injection-induced seismic emission at the KTB site, *Geophys. J. Int.* **131,** no. 2, F15–F18, doi: 10.1111/j.1365-246X.1997.tb01215.x.

Shelly, D. R., S. C. Moran, and W. A. Thelen (2013). Evidence for fluid-triggered slip in the 2009 Mount Rainier, Washington earthquake swarm, *Geophys. Res. Lett.* **40,** no. 8, 1506–1512, doi: 10.1002/grl.50354.

Sirorattanakul, K., Z. E. Ross, M. Khoshmanesh, E. S. Cochran, M. Acosta, and J. Avouac (2022). The 2020 Westmorland, California earthquake swarm as aftershocks of a slow slip event sustained by fluid flow, *J. Geophys. Res.* **127,** no. 11, e2022JB024693, doi: 10.1029/2022JB024693.

Smith, J. D., J. Avouac, R. S. White, A. Copley, A. Gualandi, and S. Bourne (2019). Reconciling the long-term relationship between reservoir pore pressure depletion and compaction in the Groningen region, *J. Geophys. Res.* **124,** no. 6, 6165–6178, doi: 10.1029/2018JB016801.

Smith, J. D., E. R. Heimisson, S. J. Bourne, and J.-P. Avouac (2022). Stress-based forecasting of induced seismicity with instantaneous earthquake failure functions: Applications to the Groningen gas reservoir, *Earth Planet. Sci. Lett.* **594,** 117697, doi: 10.1016/j.epsl.2022.117697.

Smith, J. D., Z. E. Ross, K. Azizzadenesheli, and J. B. Muir (2021). HypoSVI: Hypocentre inversion with Stein variational inference and physics informed neural networks, *Geophys. J. Int.* **228,** no. 1, 698–710, doi: 10.1093/gji/ggab309.

Smith, J. D., R. S. White, J.-P. Avouac, and S. Bourne (2020). Probabilistic earthquake locations of induced seismicity in the Groningen region, the Netherlands, *Geophys. J. Int.* **222,** no. 1, 507–516, doi: 10.1093/gji/ggaa179.

Spetzler, J., and B. Dost (2017). Hypocentre estimation of induced earthquakes in Groningen, *Geophys. J. Int.* **209,** 453–465, doi: 10.1093/gji/ggx020.

Stäuble, A. J., and G. Milius (1970). Geology of Groningen gas field, Netherlands, in *Geology of Giant Petroleum Fields*, M. Halbouty (Editor), American Association of Petroleum Geologists, 359–369, doi: 10.1306/M14368C18.

Tan, Y. J., F. Waldhauser, W. L. Ellsworth, M. Zhang, W. Zhu, M. Michele, L. Chiaraluce, G. C. Beroza, and M. Segou (2021). Machine-learning-based high-resolution earthquake catalog reveals how complex fault structures were activated during the 2016–2017 Central Italy sequence, *Seism. Record* **1,** no. 1, 11–19, doi: 10.1785/0320210001.

Trampert, J., R. Benzi, and F. Toschi (2022). Implications of the statistics of seismicity recorded within the Groningen gas field, *Neth. J. Geosci.* **101,** e9, doi: 10.1017/njg.2022.8.

Trugman, D. T., P. M. Shearer, A. A. Borsa, and Y. Fialko (2016). A comparison of long-term changes in seismicity at The Geysers, Salton Sea, and Coso geothermal fields, *J. Geophys. Res.* **121,** 225–247, doi: 10.1002/2015JB012510.

Utsu, T. (1961). A statistical study on the occurrence of aftershocks, *Geophys. Mag.* **30,** 521–605.

van der Elst, N. J. (2021). *B-Positive*: A robust estimator of aftershock magnitude distribution in transiently incomplete catalogs, *J. Geophys. Res.* **126,** no. 2, e2020JB021027, doi: 10.1029/2020JB021027.

van Thienen-Visser, K., and J. Breunese (2015). Induced seismicity of the Groningen gas field: History and recent developments, *The Leading Edge* **34,** no. 6, 664–671, doi: 10.1190/tle34060664.1.

Van Wees, J.-D., S. Osinga, K. Van Thienen-Visser, and P. A. Fokker (2018). Reservoir creep and induced seismicity: Inferences from geomechanical modeling of gas depletion in the Groningen field, *Geophys. J. Int.* **212,** no. 3, 1487–1497, doi: 10.1093/gji/ggx452.

Visser, C. A., and J. L. Solano Viota (2017). Introduction to the Groningen static reservoir model, *Neth. J. Geosci.* **96,** no. 5, s39–s46, doi: 10.1017/njg.2017.25.

Wiemer, S., and M. Wyss (2000). Minimum magnitude of completeness in earthquake catalogs: Examples from Alaska, the Western United States, and Japan, *Bull. Seismol. Soc. Am.* **90,** no. 4, 859–869, doi: 10.1785/0119990114.

Wilding, J. D., W. Zhu, Z. E. Ross, and J. M. Jackson (2023). The magmatic web beneath Hawai'i, *Science* **379,** no. 6631, 462–468, doi: 10.1126/science.ade5755.

Willacy, C., E. Van Dedem, S. Minisini, J. Li, J.-W. Blokland, I. Das, and A. Droujinine (2019). Full-waveform event location and moment tensor inversion for induced seismicity, *Geophysics* **84,** no. 2, KS39–KS57, doi: 10.1190/geo2018-0212.1.

Woessner, J., and S. Wiemer (2005). Assessing the quality of earthquake catalogues: Estimating the magnitude of completeness and its uncertainty, *Bull. Seismol. Soc. Am.* **95,** no. 2, 684–698, doi: 10.1785/0120040007.

Wu, W., D. Lu, and D. Elsworth (2022). Fluid injection-induced fault slip during unconventional energy development: A review, *Energy Rev.* **1,** no. 2, 100007, doi: 10.1016/j.enrev.2022.100007.

Yukutake, Y., K. Yoshida, and R. Honda (2022). Interaction between aseismic slip and fluid invasion in earthquake swarms revealed by dense geodetic and seismic observations, *J. Geophys. Res.* doi: 10.1029/2021JB022933.

Zaliapin, I., and Y. Ben-Zion (2013a). Earthquake clusters in southern California I: Identification and stability, *J. Geophys. Res.* **118,** no. 6, 2847–2864, doi: 10.1002/jgrb.50179.

Zaliapin, I., and Y. Ben-Zion (2013b). Earthquake clusters in southern California II: Classification and relation to physical properties of the crust, *J. Geophys. Res.* **118,** no. 6, 2865–2877, doi: 10.1002/jgrb.50178.

Zaliapin, I., and Y. Ben-Zion (2016). Discriminating characteristics of tectonic and human-induced seismicity, *Bull. Seismol. Soc. Am.* **106,** no. 3, 846–859, doi: 10.1785/0120150211.

Zaliapin, I., and Y. Ben-Zion (2020). Earthquake declustering using the nearest-neighbor approach in space-time-magnitude domain, *J. Geophys. Res.* **125,** no. 4, doi: 10.1029/2018JB017120.

Zaliapin, I., A. Gabrielov, V. Keilis-Borok, and H. Wong (2008). Clustering analysis of seismicity and aftershock identification, *Phys. Rev. Lett.* **101,** no. 1, 018501, doi: 10.1103/PhysRevLett.101.018501.

Zhai, G., M. Shirzaei, M. Manga, and X. Chen (2019). Pore-pressure diffusion, enhanced by poroelastic stresses, controls induced seismicity in Oklahoma, *Proc. Natl. Acad. Sci. Unit. States Am.* **116,** no. 33, 16,228–16,233, doi: 10.1073/pnas.1819225116.

Zhu, W., and G. C. Beroza (2019). PhaseNet: A deep-neural-network-based seismic arrival time picking method, *Geophys. J. Int.* doi: 10.1093/gji/ggy423.

Zhu, W., I. W. McBrearty, S. M. Mousavi, W. L. Ellsworth, and G. C. Beroza (2022). Earthquake phase association using a Bayesian Gaussian mixture model, *J. Geophys. Res.* **127,** no. 5, e2021JB023249, doi: 10.1029/2021JB023249.

Manuscript received 18 March 2024
Published online 5 September 2024